JM PAPERS

Boundary layer transition due to distributed roughness: effect of roughness spacing

Rong Ma[1] and Krishnan Mahesh[2],†

[1]Department of Aerospace Engineering and Mechanics, University of Minnesota, Minneapolis, MN 55455, USA

[2]Department of Naval Architecture and Marine Engineering, University of Michigan, Ann Arbor, MI 48109, USA

The influence of roughness spacing on boundary layer transition over distributed roughness elements is studied using direct numerical simulation and global stability analysis, and compared with isolated roughness elements at the same Reynolds number $Re_h = U_e h/\nu$ (U_e is the boundary layer edge velocity, h is roughness height and ν is the kinetic viscosity of the fluid). Small spanwise spacing ($\lambda_z = 2.5h$) inhibits the formation of counter-rotating vortex pairs (CVP) and, as a result, hairpin vortices are not generated and the downstream shear layer is steady. For $\lambda_z = 5h$, the CVP and hairpin vortices are induced by the first row of roughness, perturbing the downstream shear layer and causing transition. The temporal periodicity of the primary hairpin vortices appears to be independent of the streamwise spacing. Distributed roughness leads to a lower critical roughness Reynolds number for instability to occur and a more significant breakdown of the boundary layer compared with isolated roughness. When the streamwise spacing is $\lambda_x = 5h$, the high-momentum fluid barely moves downward into the cavities and the wake flow has little impact on the following roughness elements. The leading unstable varicose mode is associated with the central low-speed streaks along the aligned roughness elements, and its frequency is close to the shedding frequency of hairpin vortices in the isolated case. For larger streamwise spacing ($\lambda_x = 10h$), two distinct modes are obtained from global stability analysis. The first mode shows varicose symmetry, corresponding to the primary hairpin vortex shedding induced by the first-row roughness. The high-speed streaks formed in the longitudinal grooves are also found to be unstable and interact with the varicose mode. The second mode is a sinuous mode with lower frequency, induced as the wake flow of the first-row roughness runs into the second row. It extracts most energy from the spanwise shear between the high- and low-speed streaks.

Key words: boundary layer stability, transition to turbulence, turbulence simulation

† Email address for correspondence: krmahesh@umich.edu

1. Introduction

When laminar boundary layers encounter rough surfaces, the flow field can be greatly modified by surface roughness, and transition to turbulence can occur. Understanding roughness-induced transition is important since it leads to an increase in friction drag and affects the performance of aeronautical and naval applications. In the context of trip studies, trips in high Reynolds number flows located close to the leading edge correspond to roughness with a large h/δ^* (ratio of roughness height to the displacement boundary layer thickness). In engineering applications, moving the trip location upstream is desirable to obtain a turbulent boundary layer over a large portion of the body. However, the upstream region usually has a low Reynolds number and favourable pressure gradient, which makes it difficult to transition the flow. This, along with the boundary layer being thinner closer to the leading edge, results in a larger value of h/δ^*. See, for example, work on the DARPA SUBOFF hull by Jiménez, Reynolds & Smits (2010), Morse, Kroll & Mahesh (2022), Plasseraud *et al.* (2022) and Plasseraud, Kumar & Mahesh (2023). Three-dimensional (3-D) surface roughness can be generally categorized into isolated and distributed roughness elements, both of which are commonly involved in engineering applications. An isolated roughness element may be considered a fundamental building block for distributed roughness which is more practical. Distributed roughness elements can trigger different modes of perturbations that translate into different evolutions to a turbulent state. It is therefore important to understand the effects of spatial proximity of roughness elements, especially in the case where the following roughness elements lie within the wake of upstream elements.

The effects of isolated roughness elements on boundary layers have been studied in past literature (Baker 1979). The streamwise vortices induced by an isolated roughness element create longitudinal streaks downstream whose unstable nature plays a crucial role in the transition process (Reshotko 2001; Fransson *et al.* 2004, 2005). The linear stability properties of isolated-roughness-induced transition have been investigated both computationally and experimentally (De Tullio *et al.* 2013; Loiseau *et al.* 2014; Citro *et al.* 2015; Puckert & Rist 2018; Bucci *et al.* 2021; Ma & Mahesh 2022). They are found to depend on the combined effects of parameters such as the ratio of roughness height h to the displacement boundary layer thickness δ^*, aspect ratio $\eta = d/h$ (d is roughness width) and Reynolds number $Re_h = U_e h/\nu$ (U_e is the boundary layer edge velocity, h is roughness height and ν is the kinetic viscosity of the fluid). Compared with the isolated roughness element, distributed roughness elements display phenomena not present in the isolated case. Fewer studies have been performed on how 3-D distributed roughness elements affect the stability properties and flow structures in transitional boundary layers.

Global linear stability analysis (Theofilis 2011) provides insight into the temporal disturbance growth during the early stages of transition, and is useful for non-parallel flows such as roughness wakes. It has been used to capture and understand the leading unstable modes in boundary layer transition due to isolated roughness (Loiseau *et al.* 2014; Citro *et al.* 2015; Bucci *et al.* 2021; Ma & Mahesh 2022). The potential of global stability analysis to detect the leading unstable modes induced by distributed surface roughness remains relatively unexplored. While an isolated roughness element represents a single trip on the surface, it can also be considered a foundational model to be extended to distributed surface roughness. In this work, we therefore combine direct numerical simulation (DNS) and global stability analysis to investigate transition due to distributed surface roughness with varying streamwise and spanwise spacings, where each individual element corresponds to the geometry of isolated roughness investigated in Ma & Mahesh (2022).

Past studies of transition over distributed surface roughness have mainly focused on the effects of roughness height. Corke, Bar-Sever & Morkovin (1986) studied the effects of distributed roughness on transition and suggested that transition is most likely to be triggered by the few highest peaks. They also found that the low-inertia fluid in the valleys between roughness elements could be influenced more easily by free-stream disturbances. For roughness with small amplitudes, transition is induced through a linear amplification of temporal disturbance growth followed by secondary instabilities and breakdown to turbulence (Reshotko 2001). In contrast, large-amplitude roughness creates local separations, leading to strong 3-D disturbances that can develop into turbulence directly. This is the so-called 'bypass' transition, which means that the linear instability processes such as Tollmien–Schlichting waves are bypassed. Vadlamani, Tucker & Durbin (2018) conducted numerical investigations on the transition of a subsonic boundary layer over distributed surface roughness with different heights. They suggested that secondary instabilities on the streaks promote the transition to turbulence for roughness elements that are inside the boundary layer and that the instability wavelengths appear to be governed by the fixed streamwise and spanwise spacings between roughness elements. For roughness elements that are higher than the boundary layer, they found that the scale of instability is shorter and the shedding from the obstacles leads to transition. von Deyn *et al.* (2020) investigated the influence of distributed roughness and free-stream turbulence on bypass transition. They found that the bypass transition occurs as a result of the secondary instability of low-speed streaks and suggested that the streak spacing does not vary with different roughness densities at constant roughness height.

While roughness height is an important parameter to affect transition, roughness spacing can also potentially modify the transitional flow behaviour and associated instability mechanisms. Investigation of spanwise proximity of roughness elements has commonly involved spanwise arrays of roughness elements. Ergin & White (2006) studied transitional flow behind a spanwise array of cylindrical roughness elements and suggested that transition results from a competition between unsteady disturbance growth and steady disturbance decay. Choudhari & Fischer (2006) performed numerical simulations of a flat plate boundary layer past a spanwise array of cylindrical roughness elements (spaced three diameters away from each other). They observed self-sustained and unsteady vortical structures that resemble the flow structures during natural transition for roughness with large height. Muppidi & Mahesh (2012) investigated supersonic boundary layer flow over distributed surface roughness and showed that the counter-rotating vortex pairs induced by roughness perturb the shear layer and trigger transition. With closely packed roughness elements, there is little upstream spacing to generate a strong horseshoe vortex and little spanwise spacing to produce counter-rotating vortices, which can prevent the transition from occurring. The influence of spanwise spacing on instability and transition has been less explored in past work. Our present study aims to quantitatively evaluate the effects of spanwise spacing of roughness elements on the vortical structures and associated instability characteristics in transition.

The role of the streamwise proximity of the roughness elements is also a crucial factor of transition due to distributed roughness. Choudhari *et al.* (2010) performed simulations of a high-speed boundary layer past an isolated diamond trip as well as two trips aligned with the flow direction (spaced at three times the trip width). They found that the introduction of an additional trip could amplify the streak amplitude and cause transition even at a smaller trip height, while the case with a larger trip height presents a weaker augmentation of the streak amplitude since the flow has not recovered as much as for smaller trip height. In a turbulent boundary layer, the classification of d-type and k-type behaviours (Jiménez 2004) is related to the streamwise roughness spacing and might be made based on the

ratio of roughness pitch to height being equal to 3 (Tani 1987). Perry, Schofield & Joubert (1969) and Ikeda & Durbin (2007) further claimed that the difference between k-type and d-type roughness is related to the state of vortex shedding: for d-type roughness, stable vortices form within the grooves and no eddy sheds into the flow above the crests; for k-type roughness, eddies with a length scale of order *h* shed into the flow above the crests. Vanderwel & Ganapathisubramani (2015) suggested that distributed roughness with streamwise gaps less than (4–5)*h* would act like continuous strips in turbulent boundary layers, while more than 5*h* would act like 3-D distributed roughness. Although the dependence of flow behaviours on different streamwise spacings has been discussed extensively in turbulent boundary layers, less studied is how streamwise spacing affects transition. This work, therefore, investigates transition due to distributed surface roughness with streamwise spacing 5*h* and 10*h* and compares the results with the isolated roughness case.

The paper is organized as follows. The numerical methodology is introduced in § 2. The flow configuration and simulation details are discussed in § 3. In § 4, the influence of distributed roughness on the transitional boundary layer is studied, the formation mechanisms of hairpin vortices in different roughness distributions are examined, and the base flow and global stability results are analysed and compared with the isolated case. Finally, the paper is summarized in § 5.

2. Numerical methodology

The governing equations and numerical methods are briefly summarized. An overview of linear stability and details regarding the iterative eigenvalue solver are provided.

2.1. *Direct numerical simulation*

The incompressible Navier–Stokes (N–S) equations are solved using the finite volume algorithm developed by Mahesh, Constantinescu & Moin (2004)

$$\frac{\partial u_i}{\partial t} + \frac{\partial}{\partial x_j}(u_i u_j) = -\frac{\partial p}{\partial x_i} + \nu \frac{\partial^2 u_i}{\partial x_j x_j} + K_i, \quad \frac{\partial u_i}{\partial x_i} = 0, \quad\quad (2.1a,b)$$

where u_i and x_i are the *i*th components of the velocity and position vectors, respectively, *p* denotes pressure divided by density, ν is the kinematic viscosity of the fluid and K_i is a constant pressure gradient (divided by density). Note that the density is absorbed in the pressure and K_i. The algorithm is robust and emphasizes discrete kinetic energy conservation in the inviscid limit which enables it to simulate high-*Re* flows without adding numerical dissipation. A predictor–corrector methodology is used where the velocities are first predicted using the momentum equation and then corrected using the pressure gradient obtained from the Poisson equation yielded by the continuity equation. The Poisson equation is solved using a multigrid pre-conditioned conjugate gradient method using the Trilinos libraries (Sandia National Labs).

The DNS solver has been validated in Ma, Alamé & Mahesh (2021) for a smooth turbulent channel flow, and a rod-roughened turbulent channel flow. Good agreement is obtained for the mean velocity and Reynolds stresses profiles with the DNS results of Moser, Kim & Mansour (1999) and Ashrafian, Andersson & Manhart (2004).

2.2. *Linear stability analysis*

Modal linear stability analysis is the study of the dynamic response of a base state subject to infinitesimal perturbations (Theofilis 2011). In the present work, the incompressible N–S equations (2.1*a,b*) are linearized about a base state, $\bar{u}_i$ and $\bar{p}$. The flow can be decomposed into a base state subject to a small $O(\epsilon)$ perturbation $\tilde{u}_i$ and $\tilde{p}$. The linearized Navier–Stokes (LNS) equations are obtained by subtracting the base state from (2.1*a,b*) and neglecting the nonlinear terms. It can be written as follows:

$$\frac{\partial \tilde{u}_i}{\partial t} + \frac{\partial}{\partial x_j}\tilde{u}_i\bar{u}_j + \frac{\partial}{\partial x_j}\bar{u}_i\tilde{u}_j = -\frac{\partial \tilde{p}}{\partial x_i} + \nu \frac{\partial^2 \tilde{u}_i}{\partial x_j x_j}, \quad \frac{\partial \tilde{u}_i}{\partial x_i} = 0. \qquad (2.2a,b)$$

The same numerical schemes as the N–S equations are used to solve the LNS equations. Periodic boundary conditions are imposed on the spanwise domain boundaries. Homogeneous Dirichlet boundary conditions are used at the inlet, the upper boundary and the bottom walls, while the convective boundary condition is used at the outflow boundary.

The LNS equations can be rewritten as a system of linear equations

$$\frac{\partial \tilde{u}_i}{\partial t} = \boldsymbol{A}\tilde{u}_i, \qquad (2.3)$$

where A is the LNS operator and $\tilde{u}_i$ is the velocity perturbation. The solutions to the linear system of (2.3) are

$$\tilde{u}_i(x, y, z, t) = \sum_{\omega} \hat{u}_i(x, y, z)\mathrm{e}^{\omega t}, \qquad (2.4)$$

where $\widehat{u_i}$ is the velocity coefficient, and both $\widehat{u_i}$ and ω can be complex. This defines $\sigma = Re(\omega)$ as the growth/damping rate and $\omega_a = Im(\omega)$ as the temporal frequency of $\widehat{u_i}$. The linear system of equations can then be transformed into a linear eigenvalue problem

$$\boldsymbol{\Omega}\hat{U} = \boldsymbol{A}\hat{U}, \qquad (2.5)$$

where $\omega_j = \mathrm{diag}(\boldsymbol{\Omega})_j$ is the jth eigenvalue and $\hat{U}$ is the matrix of eigenvectors. For global stability analysis, solving the eigenvalue problem using direct methods is very computationally expensive. Instead, a matrix-free method, the implicitly restarted Arnoldi method implemented in the PARPACK library is used to efficiently solve for the leading eigenvalues and eigenmodes in the present work.

3. Simulation details

Figure 1 depicts the flow configuration and roughness distribution. On the flat plate, attached cuboids with an aspect ratio of width to height $\eta = d/h = 1$ are aligned in both the streamwise and spanwise directions. The collocated distribution is chosen because the study is focused on understanding the effects of the spatial proximity of the roughness elements, especially in the case where the following roughness lies within the wake of upstream elements. For the staggered configuration, the following elements are possibly not located within the roughness wakes of the first-row elements. They will have a larger initial δ^*/h and therefore may induce different types of perturbation modes. The ratio of the displacement boundary layer thickness to the first-row roughness height is $\delta^*/h = 0.35$, consistent with the isolated cube in Ma & Mahesh (2022). The roughness height is $h = 1$, the reference length in the simulations. The Blasius laminar boundary layer solution is specified at the inflow boundary, and convective boundary conditions
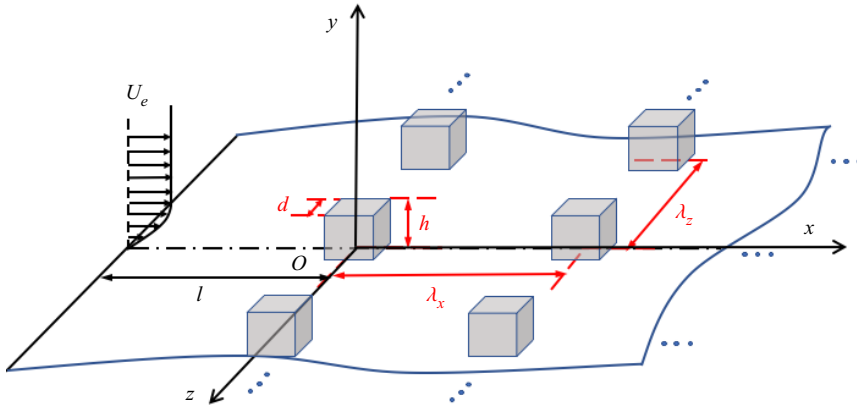
Figure 1. Schematic of the flow configuration and roughness distribution. The x, y and z coordinates are the streamwise, wall-normal and spanwise directions. The distance from the inlet of the computational domain to the first row of roughness elements remains constant at $l = 15h$. The streamwise and spanwise spacings are denoted by λ_x and λ_z, respectively.

Case	λ_x	λ_z	$N_x \times N_y \times N_z$	$L_x \times L_y \times L_z$	Δx^+, Δz^+	Δy^+_{wall}	Δy^+_{top}
isolated	—	—	$1080 \times 240 \times 240$	$45h \times 15h \times 10h$	0.72–2	0.24–0.36	12.6
$(5h, 2.5h)$	$5h$	$2.5h$	$1860 \times 240 \times 240$	$77.5h \times 15h \times 10h$	0.72–2	0.24–0.36	12.6
$(5h, 5h)$	$5h$	$5h$	$1860 \times 240 \times 240$	$77.5h \times 15h \times 10h$	0.72–2	0.24–0.36	12.6
$(10h, 5h)$	$10h$	$5h$	$2160 \times 240 \times 240$	$90h \times 15h \times 10h$	0.72–2	0.24–0.36	12.6

Table 1. Simulation parameters for the isolated and distributed roughness cases at $Re_h = 600$.

are used at the outflow boundary. Periodic boundary conditions are used in the spanwise direction. No-slip boundary conditions are imposed on the flat plate and the roughness surfaces. The boundary conditions $U_e = 1$, $\partial v/\partial y = 0$ and $\partial w/\partial y = 0$ are used at the upper boundary. Uniform grids are used in the streamwise and spanwise directions, and the grid in the wall-normal direction is clustered near the flat plate. Three distributed roughness cases with different λ_x and λ_z are investigated at $Re_h = 600$ in the present work. The grid size and domain length are determined based on the grid convergence and domain length sensitivity studies in Ma & Mahesh (2022) for an isolated cube with a similar flow configuration. They are also comparable to past literature on flow simulations over cube roughness (Coceal *et al.* 2006; Leonardi & Castro 2010; Xu *et al.* 2021). Details of domain length and grid information are shown in table 1.

4. Results

4.1. *Distributed roughness effects on boundary layers*

Different roughness spacing affects boundary layer behaviour. The wake flow downstream of the roughness elements is visualized by instantaneous streamwise velocity in the symmetry plane in figure 2. Figure 2(*a*) shows that, for case $(5h, 2.5h)$, the reverse
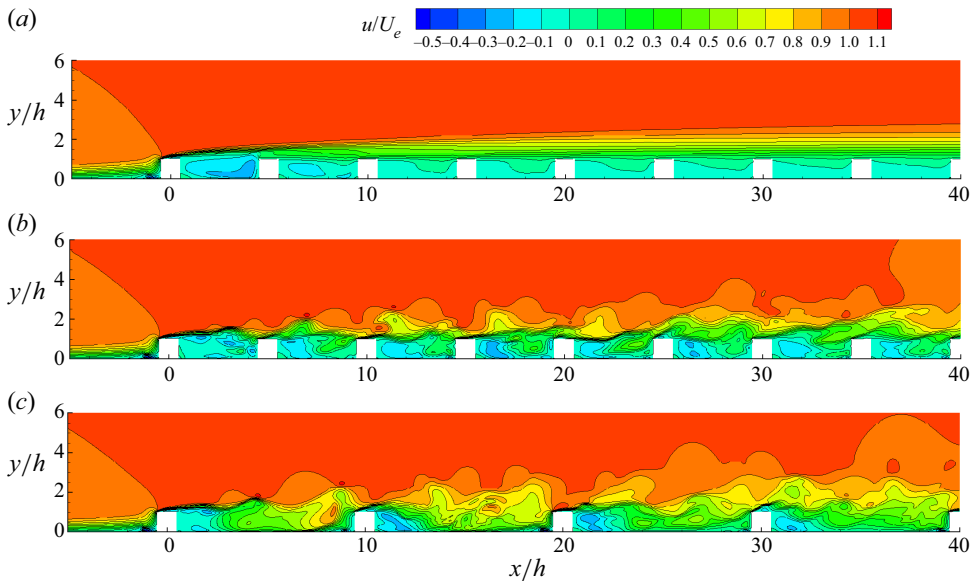
977 A27-6

Figure 2. Instantaneous streamwise velocity u/U_e in the symmetry plane from the DNS at $Re_h = 600$ for (*a*) case $(5h, 2.5h)$, (*b*) case $(5h, 5h)$ and (*c*) case $(10h, 5h)$.

flow is strong in the first cavity and becomes weak from the second cavity onwards. Wall-normal momentum transfer hardly occurs and the boundary layer above the roughness layer remains laminar. According to Castro & Robins (1977) and Vanderwel & Ganapathisubramani (2015), roughness with gaps of less than $(4–5)h$ would act more like continuous strips. They sustain recirculation vortices that isolate the outer flow from the roughness, as observed for case $(5h, 5h)$ in figure 2(*b*). In contrast, roughness with longer gaps induces recirculation bubbles that reattach ahead of the next cubes, and the outer flow penetrates into the cavities. For a larger streamwise spacing $\lambda_x = 10h$, as shown in figure 2(*c*), the high-momentum fluid transfers downwards into the first cavity and impinges on the second-row roughness. The penetration of high-momentum fluid into the cavities becomes weaker with increasing downstream distance. The unsteadiness of the roughness wake flow is depicted by the streamwise velocity fluctuations for cases $(5h, 5h)$ and $(10h, 5h)$ in figure 3. For case $(5h, 5h)$, the strong velocity fluctuations occur at the localized shear layers induced by the roughness elements. The low level of fluctuations in the cavities indicates that the recirculation bubbles located within the cavities remain quite steady. For case $(10h, 5h)$, the large value of root-mean-square streamwise velocity fluctuations u_{rms} is observed in front of the second-row elements, possibly due to the vortex shedding into the cavities. The large fluctuations are not observed above the second-row elements, indicating that, as the wake flow of the first-row elements impinges the second row, different perturbation modes may be induced. The detailed vortical structures and their associated instability will be examined in §§ 4.2 and 4.3.

The effect of streamwise roughness spacing on transitional boundary layers is examined through boundary layer integral parameters for cases $(5h, 5h)$ and $(10h, 5h)$, with a comparison with the isolated cube. The streamwise variation of the displacement boundary layer thickness (δ^*), momentum boundary layer thickness (θ) and shape factor (H) is presented in figures 4(*a*)–4(*c*). The parameters are computed from a time-averaged flow field and spanwise averaging is performed across the span. Comprehensive spatial
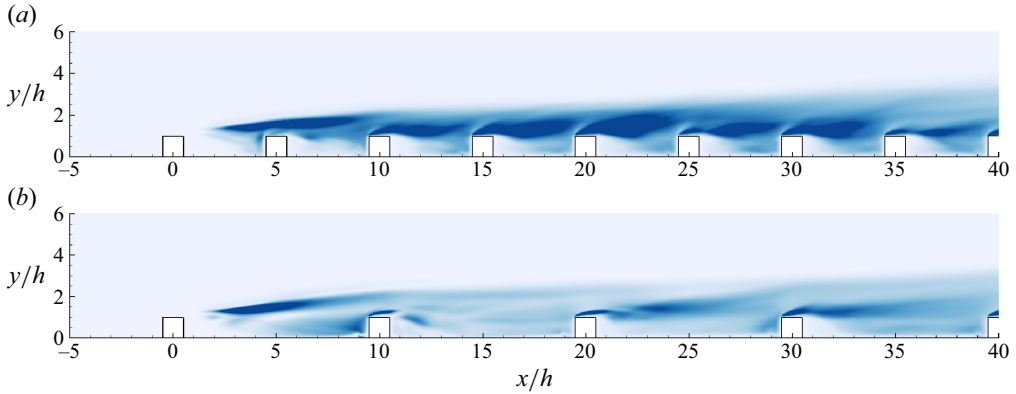
Figure 3. Streamwise velocity fluctuations u_{rms}/U_e in the symmetry plane from the DNS at $Re_h = 600$ for (*a*) case (5*h*, 5*h*) and (*b*) case (10*h*, 5*h*). The contours are from 0 (white) to 0.03 (blue).
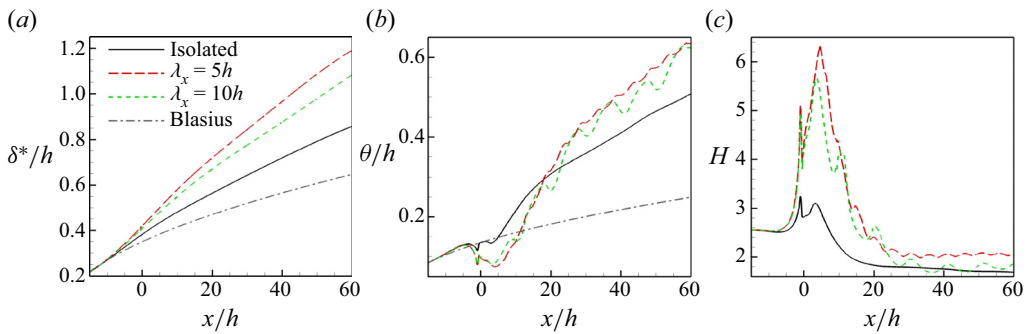

Figure 4. Streamwise variations of (*a*) displacement boundary layer thickness, (*b*) momentum boundary layer thickness and (*c*) shape factor of cases (5*h*, 5*h*) and (10*h*, 5*h*) at $Re_h = 600$, and comparison with the isolated roughness and laminar Blasius solution.

averaging, where the averaging volume includes both the fluid and solid area, is used to ensure continuity in the profiles (Xie & Fuka 2018). To understand the spatial inhomogeneity of the flow field caused by distributed roughness, the local integral boundary layer parameters are also shown in figure 5.

In figure 4(*a*), an increase in δ^* is seen due to the presence of roughness elements compared with the laminar Blasius solution. A more significant increase is observed for distributed roughness than the isolated roughness. The increase is more pronounced for distributed roughness with smaller λ_x since the denser streamwise roughness distribution leads to stronger perturbations to the downstream shear layer. This can also be confirmed by the fluctuations examined in figure 3. Figure 5(*a*) shows that the region with lower values of local δ^* corresponds to the location of lateral high-speed streaks induced by roughness. Figure 4(*b*) shows a negative deviation from the Blasius solution in the profiles of θ for the distributed roughness cases. This is related to the strong reverse flow that occurs closely behind the first two rows of roughness elements, as demonstrated by figure 5(*b*). A steeper increase in the profiles of θ indicates that the breakdown of boundary layers is more significant for distributed surface roughness compared with the isolated roughness.
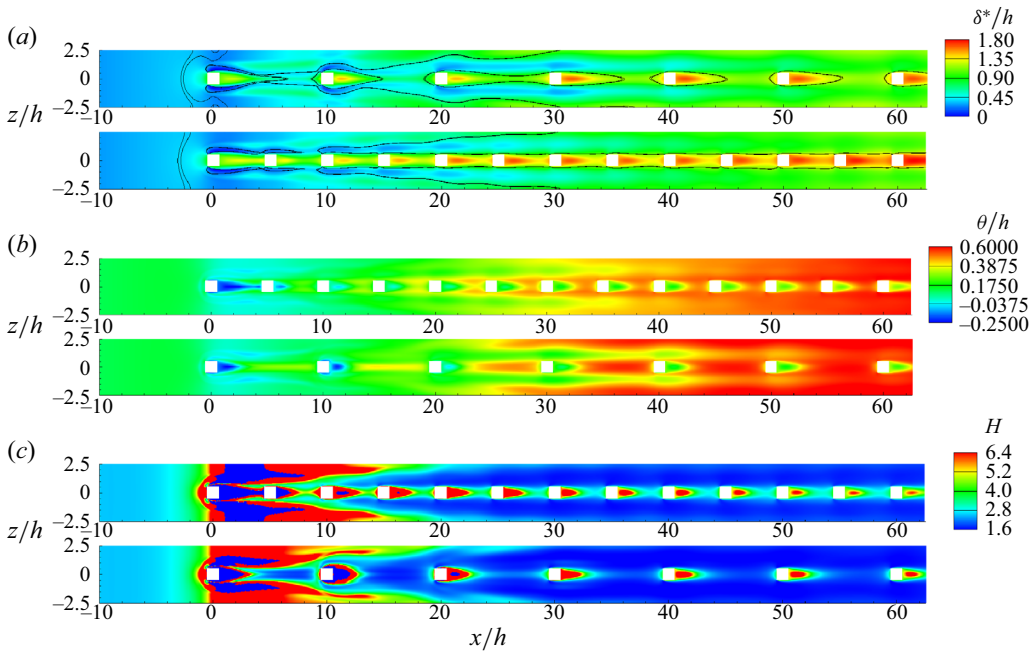
977 A27-8

Figure 5. Contour plots of the local integral boundary layer parameters (*a*) displacement boundary layer thickness, (*b*) momentum boundary layer thickness and (*c*) shape factor for cases $(5h, 5h)$ and $(10h, 5h)$ at $Re_h = 600$. The lateral high-speed streaks are depicted by the solid contour lines in (*a*) using the streamwise velocity deviation of the mean flow from the Blasius solution.

The shape factor in figure 4(*c*) shows a significant increase compared with the isolated roughness. The high values of H are associated with inflection points and reveal locally the instability of the streaks induced by roughness elements, as shown in figure 5(*c*). The steep drop in H begins at approximately $x = 5h$ for the three cases, suggesting that the streaks with high amplitudes break down and transition happens at similar downstream positions for three different roughness distributions. The shape factor converges farther downstream after the breakdown. The values are higher for case $(5h, 5h)$ when compared with case $(10h, 5h)$ and the isolated case, resulting from a stronger blockage effect of a denser roughness distribution.

4.2. *Formation and evolution of hairpin-shaped vortices*

Packets of hairpin-shaped vortices are key structures in roughness-induced transition. They are associated with global instability, as known for isolated roughness. Cohen, Karp & Mehta (2014) proposed a model consisting of three key elements required for the formation of hairpin vortices: simple shear, counter-rotating vortices and a 2-D vortex sheet, and highlight that this combination is unstable. It is therefore important to understand the influence of roughness spacing on the generation and evolution of hairpin vortices in roughness wakes.

4.2.1. *Counter-rotating vortex pairs (CVP)*

As known for isolated roughness, the spanwise vortices formed upstream wrap around the roughness element and give birth to the streamwise vortices downstream of the roughness,
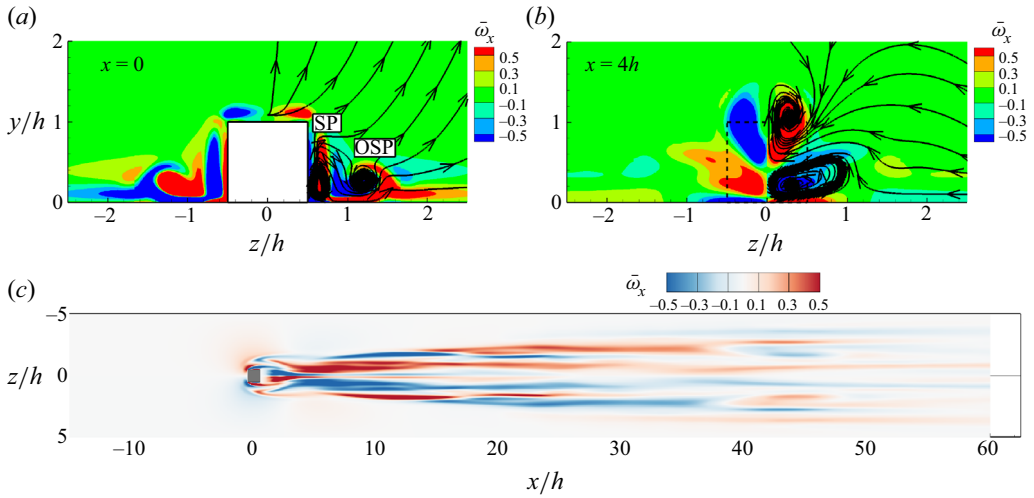
Figure 6. Mean streamwise vorticity $\bar{\omega}_x = \pm 0.5$ with mean streamlines in the cross-flow planes (a,b) and the plane of $y = 0.5h$ (c) from the DNS at $Re_h = 600$ for the isolated roughness.

and the streamwise counter-rotating vortices are known to play a critical role in the generation of hairpin vortices (Iyer & Mahesh 2013; Bucci *et al.* 2021). As the baseline, figure 6 depicts the characteristics of streamwise vortices induced by an isolated cube. The symmetry plane (SP) vortices located very close to the roughness have an upwash between them. They lift up and move towards each other with increasing downstream distance, and are dissipated at $x = 25h$. The off-symmetry plane (OSP) vortices located farther from the SP are the continuation of the vortex tubes from upstream. They have a central downwash which keeps them away from each other with increasing downstream distance.

The effects of spanwise spacing on CVP are investigated for case $(5h, 2.5h)$ in figure 7. At $x = 0$, the OSP vortices are observed in the groove between two adjacent cubes, similar to the isolated case. However, the SP vortices do not appear on either side of the obstacles, in contrast to the isolated case. The generation mechanism of the SP vortices is examined using the mean streamlines in figure 7(a) and illustrated in figure 7(b). The secondary flow close to the cube sides moves downward due to the motion of the OSP vortices (from a to b), then moves toward the cube due to a positive spanwise pressure gradient (from b to c), and moves upward for mass conservation (from c to d). With small spanwise spacing, the OSP vortices in the groove are located closer to each other, which strengthens the upward fluid motion in the groove and weakens the centrifugal forces. The last step under the effects of centrifugal forces for the generation of SP vortices (from d to a) is therefore missing. As a result, a weak CVP is observed at the roughness tip location at $x = 4h$ and is dissipated within a short downstream distance. The OSP vortices in the groove are also diminished with increasing downstream distance and mostly disappear beyond the second row of roughness elements, as shown in figure 7(c).

The effects of streamwise spacing on CVP are investigated in figure 8 for cases $(5h, 5h)$ and $(10h, 5h)$. For both cases, the SP and OSP vortices are observed and behave similarly to the isolated roughness at $x = 0$. Figure 8(a) shows that, for case $(5h, 5h)$, the CVP grows with increasing downstream distance, and is distorted and pushed apart by the following roughness as observed at $x = 4h$. At $x = 10h$, the SP vortices developed from the front obstacles are weakened due to the stagnation effects of the following obstacles, but a new pair of SP vortices is induced again on either side of the cube, and the OSP vortices on
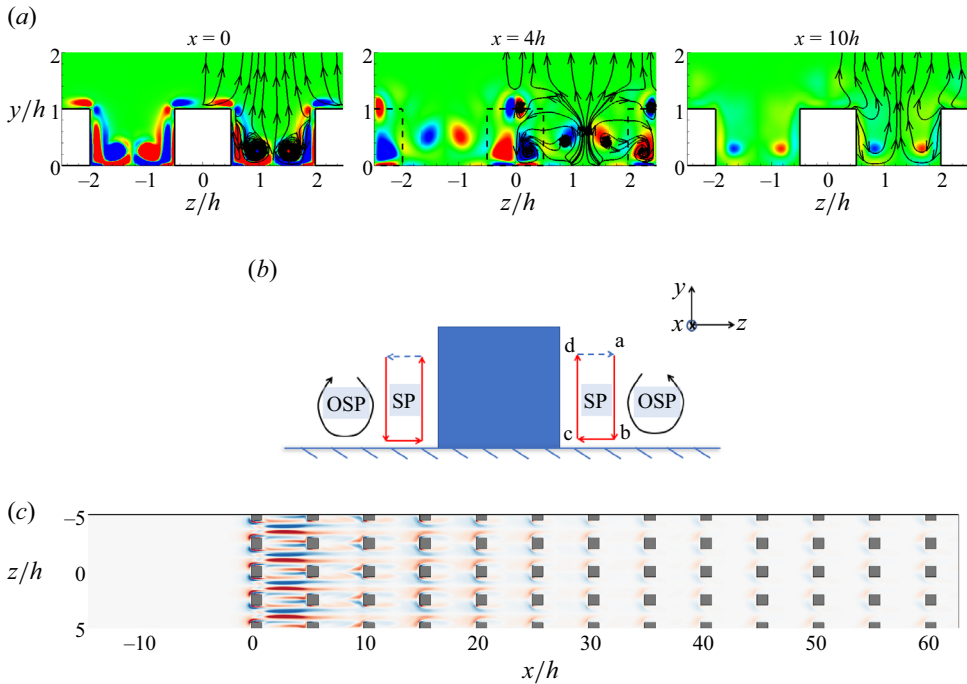
977 A27-10

Figure 7. (*a*) Mean streamwise vorticity $\bar{\omega}_x = \pm 0.5$ with mean streamlines in the cross-flow planes, (*b*) illustration of the formation mechanisms of SP vortices and (*c*) streamwise evolution of $\bar{\omega}_x$ at the plane of $y = 0.5h$ from the DNS of case ($5h$, $2.5h$) at $Re_h = 600$. The contour levels are the same as figure 6.

the lateral sides are strengthened. Figure 8(*c*) shows that the CVP is dissipated beyond $x = 30h$, similarly to the isolated roughness case.

For case ($10h$, $5h$), the streamwise spacing is much larger than the streamwise length of the separation region. The behaviour of the CVP is similar to that for an isolated roughness at $x = 0$ and $4h$, as shown in figure 8(*b*). Instead of being distorted by the roughness as case ($5h$, $5h$), both the SP and OSP vortices move closer to the SP, enhancing the momentum exchange within the cavities. At $x = 10h$, they impinge onto the second row of roughness elements and break down into small vortical structures. A new pair of SP vortices is generated and the OSP vortices are strengthened on the lateral sides. Figure 8(*d*) shows that, after the second-row cubes, the SP vortices are maintained in the cavities while the OSP vortices develop in the longitudinal grooves. The CVP persists farther than case ($5h$, $5h$), and is dissipated beyond $x = 40h$.

4.2.2. *Roughness wake flow*

The CVP examined in §4.2.1 perturbs the shear layer in its vicinity, and its size and strength determines the nature of the perturbation to the shear layer and the characteristics of roughness wakes. To understand how multiple roughness elements affect the evolution of hairpin vortices in roughness wakes and the wake extension, the instantaneous spanwise vorticity and mean streamwise velocity at the SP are visualized in figures 9 and 10, respectively. The wake flow downstream of the isolated cube is shown as the baseline in figure 9(*a*). The breakdown of the shear layer is observed downstream of the cube due to the perturbation of vortex shedding, and the vortex heads are largely dissipated by $x = 20h$.
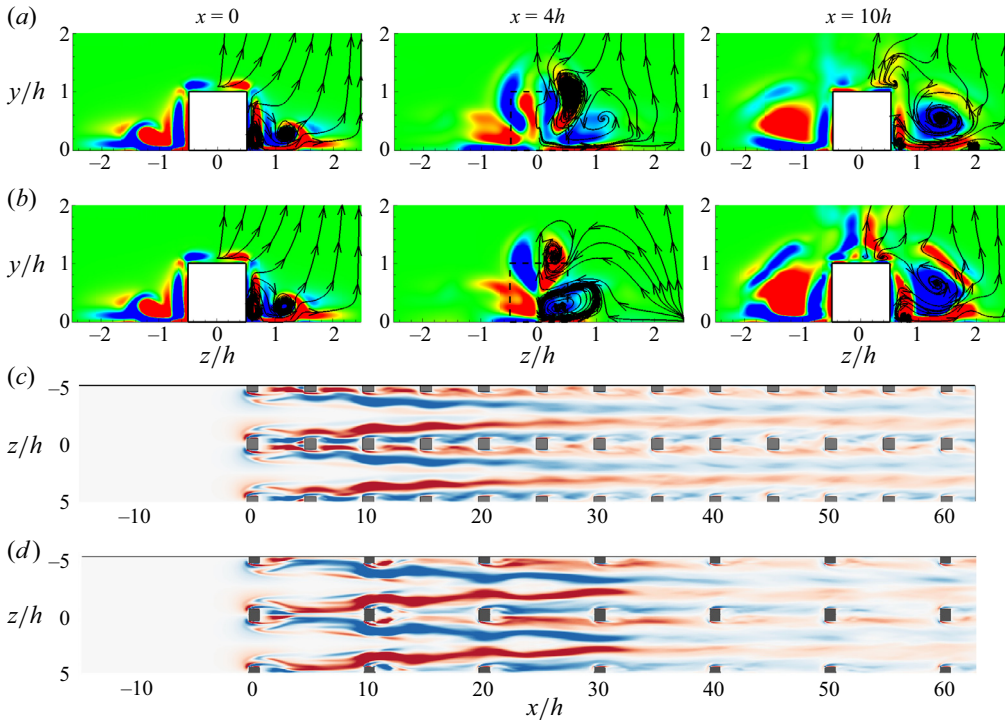
977 A27-11

Figure 8. Mean streamwise vorticity $\bar{\omega}_x = \pm 0.5$ with mean streamlines in the cross-flow planes and the plane of $y = 0.5h$ from the DNS at $Re_h = 600$ for (*a,c*) case ($5h$, $5h$) and (*b,d*) case ($10h$, $5h$). The contour levels are the same as figure 6.

For distributed surface roughness, figure 9(*b*) shows that, for small spanwise spacing $\lambda_z = 2.5h$, the downstream shear layer forms right above the roughness tips and no hairpin-shaped vortex shedding is produced in the wake flow. The inflection point in the mean velocity profiles is examined in figure 11. It is a necessary condition for instability in shear flows and corresponds to the peak location of spanwise vorticity. Although the inflection points formed by wall-normal shear can be identified for case ($5h$, $2.5h$) in figure 11, the absence of CVP due to the small spanwise spacing results in a failure of hairpin vortex generation. As a consequence, the perturbation to the shear layer is weak, and a stable shear layer is formed above the roughness layer.

With larger spanwise spacing $\lambda_z = 5h$, the disturbances present in the roughness wake can trigger strong nonlinear interactions, leading to the breakdown of the shear layer, as observed in figures 9(*c*) and 9(*d*). Figure 10 shows the modification of different λ_x to the roughness wake flow, with a comparison with the isolated case. Multiple roughness elements lead to a wake extension by generating recirculation bubbles in the wake flow. Distributed roughness in case ($5h$, $5h$) sustains recirculation bubbles that isolate the outer flow from the roughness layer, as observed in figure 10(*b*). As a result, although the primary hairpin vortices that behave similarly to the isolated case can be identified above the roughness tips in figure 9(*c*), they rarely shed into the roughness layer. Meanwhile, the following roughness elements persistently induce disturbances to the roughness wake, as shown by the localized shear layers induced right above each element (red regions in figure 9*c*). These localized shear layers that contain high-level fluctuations contribute to the unstable nature of the roughness wake.
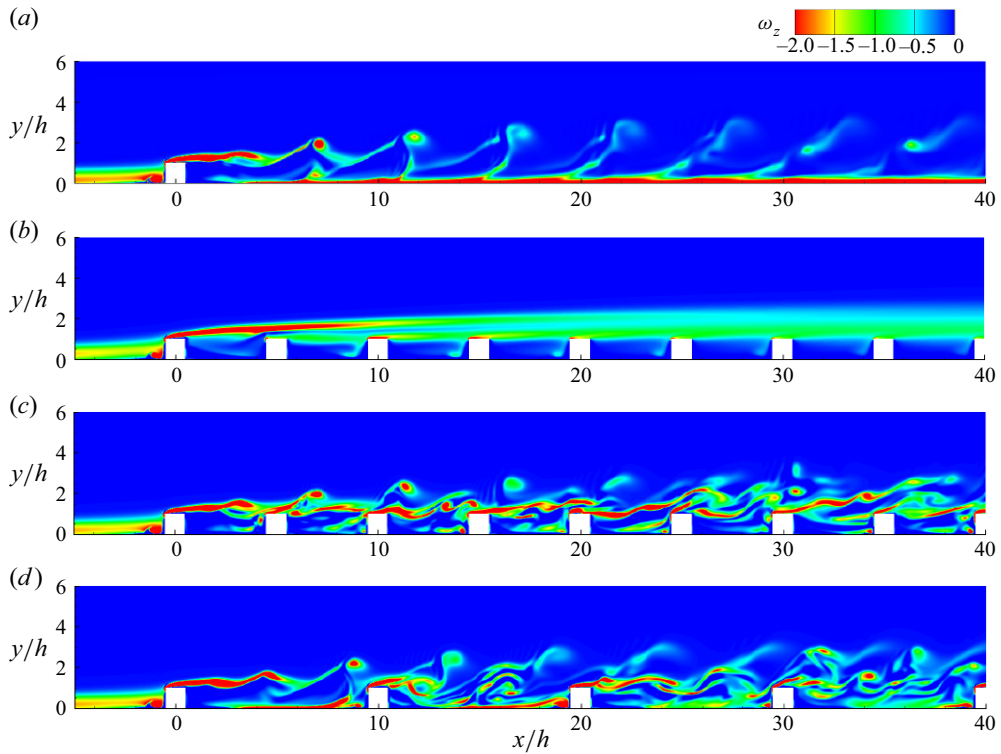
977 A27-12

Figure 9. Instantaneous spanwise vorticity in the SP from the DNS at $Re_h = 600$ for (*a*) isolated roughness, (*b*) case $(5h, 2.5h)$, (*c*) case $(5h, 5h)$ and (*d*) case $(10h, 5h)$.
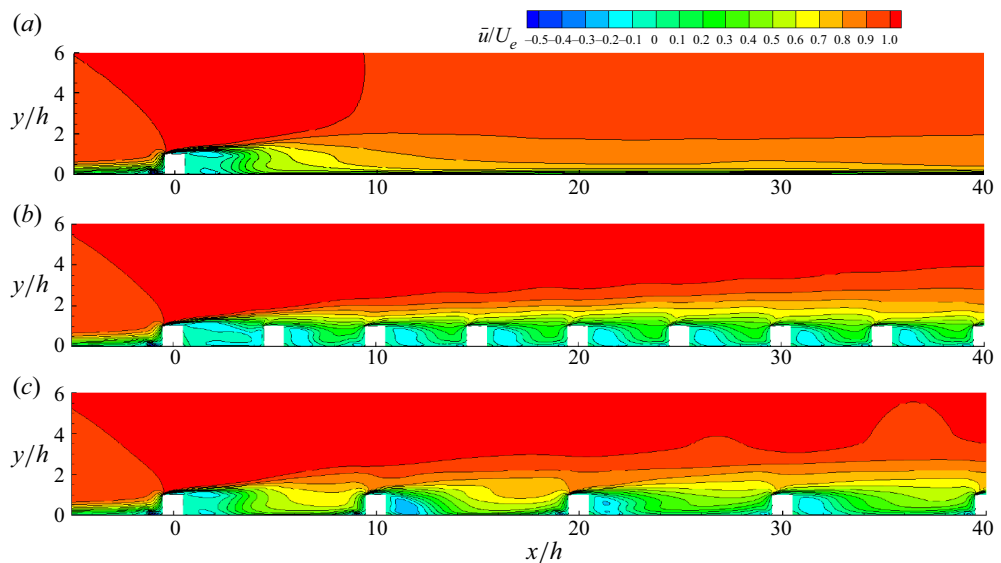

Figure 10. Mean streamwise velocity $\bar{u}/U_e$ in the SP from the DNS at $Re_h = 600$ for (*a*) the isolated case, (*b*) case $(5h, 5h)$ and (*c*) case $(10h, 5h)$.
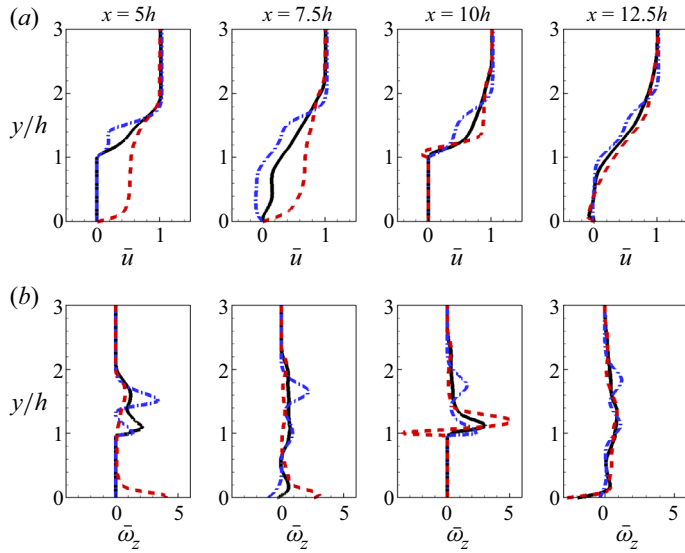
Figure 11. Streamwise variation of (*a*) $\bar{u}$ and (*b*) $\bar{\omega}_z$ profiles in the SP for case ($5h$, $5h$) (black solid), case ($5h$, $2.5h$) (blue dash-dot) and case ($10h$, $5h$) (red dashed) at $Re_h = 600$.

In contrast, roughness with longer gaps (case ($10h$, $5h$)) induces recirculation bubbles that reattach ahead of the next cubes, and the outer flow penetrates into the cavities. In figure 10(*c*), the recirculation region is similar to the isolated case, but the high-momentum fluid transfers downwards into the first cavity, and the wake flow impacts the following elements. It is also observed that the penetration of high-momentum fluid into the cavities becomes weaker with increasing downstream distance. In figure 9(*d*), the hairpin vortex shedding induced by the first row of elements behaves similarly to the isolated case. However, more complex vortical structures evolve into the cavities from the second-row cubes as the wake flow impinges onto the following elements. Although different roughness distributions modify roughness wake flow, the periodicity of the primary hairpin vortex shedding seems to be consistent with that of the isolated roughness and independent of the streamwise roughness spacing. The associated instability mechanisms will be further examined and discussed in § 4.3.

The evolution of the primary vortical structures in roughness wakes is examined for cases ($5h$, $5h$) and ($10h$, $5h$) using the Q criterion which defines vortices as areas where the vorticity magnitude is greater than the magnitude of the rate of strain (Hunt, Wray & Moin 1988). For case ($5h$, $5h$) in figure 12, both the SP and OSP vortices are observed in the vicinity of the first-row cubes. They interact with the shear layer, leading to the hairpin vortex shedding downstream of the first-row roughness elements. The packets of hairpin-type structures with small legs labelled 1 can be identified from the top-down view. The shorter streamwise extent of the vortical motions is due to the blockage effects of the closely distributed cubes. As the vortex legs are inclined upward and undergo stretching by a positive wall-normal velocity gradient, they are cut off by the following cubes and break down into smaller vortical structures with low momentum within the roughness layer. The interactions between vortical structures in the longitudinal grooves occur at approximately $x = 15h$, and the arch-shaped vortical structures are observed farther downstream.

For case ($10h$, $5h$), both SP and OSP vortices are observed, and the hairpin vortices are generated from the first-row cubes, as shown in figure 13. The top-down view shows that
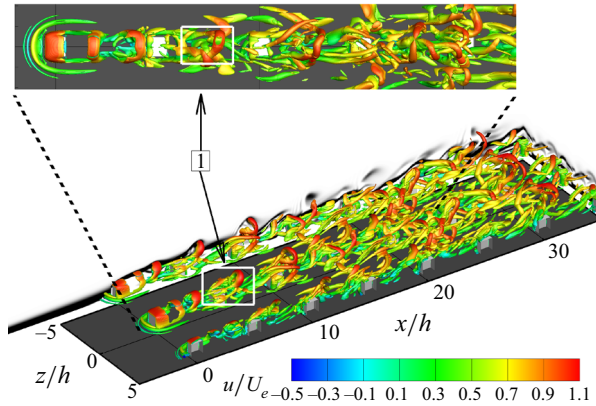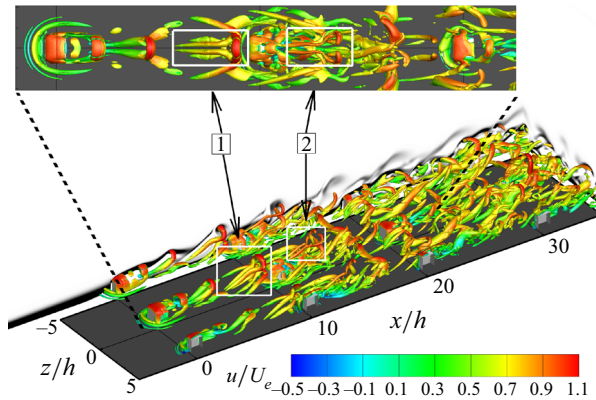
Figure 12. Instantaneous vortical structures for case $(5h, 5h)$ in perspective and top-down views, visualized by isocontours of $Q = 0.1U_e^2/h^2$ and coloured with instantaneous streamwise velocity. Plotted in the x–y and z–y planes are the contours of instantaneous spanwise vorticity, in the range of -1 (black) and 0 (white).

Figure 13. Instantaneous vortical structures for case $(10h, 5h)$ in perspective and top-down views, visualized by isocontours of $Q = 0.1U_e^2/h^2$ and coloured with instantaneous streamwise velocity. The contour levels are the same as figure 12.

the hairpin vortices labelled 1 behave similarly to the isolated roughness case. In contrast to the cut off vortex legs observed in case $(5h, 5h)$, the primary hairpin vortices in case $(10h, 5h)$ have sufficient space to develop downstream. However, as the high-momentum fluid impinges onto the second-row elements, another spanwise vortex wraps around the second-row cubes (see the vortical structures in green), and the vortical structures break down into small scales downstream of the second-row cubes. The CVP sheds from the second-row roughness tips, and the hairpin-like vortices with a separation of the vortex heads labelled 2 are observed. This indicates that a different unstable mode might be induced by the second-row elements in case $(10h, 5h)$.

4.3. *Global stability analysis*

The hairpin vortices induced by roughness elements are inherently unstable as the CVP perturbs the shear layer, forming the inflection point in the base-flow velocity profiles. The perturbation of the shear layer is inhomogeneous in the spanwise direction and therefore

the global stability analysis is useful to provide insights into the instability mechanisms associated with the distributed roughness wakes.

4.3.1. *Base-flow computation*

The base flow for global instability analysis is computed for the distributed roughness cases. For cases (5*h*, 2.5*h*) and (5*h*, 5*h*), the selective frequency damping (SFD) method (Åkervik *et al.* 2006) is used to artificially settle the flow towards a steady equilibrium. An encapsulated formation of the SFD method developed by Jordi, Cotter & Sherwin (2014) is applied in the present work.

For case (10*h*, 5*h*), it is found that the SFD method is unable to damp the oscillations due to the unsteady part of the solutions, even though careful choices are made for the control coefficient χ and the filter width Δ. The possible reason is that the SFD method is unable to get the steady state when there are multiple unstable modes, as indicated by Casacuberta *et al.* (2018). They discussed the effectivity of SFD for systems with more than one unstable eigenmode where the most unstable eigenvalue is μ^c and other unstable eigenvalues are denoted by μ^k. They concluded that SFD is unable to drive the system towards the base flow when μ^k with large values of $Im(\mu^k)/Re(\mu^k)$ is present close to the origin. As discussed in Ma & Mahesh (2022), using the time-averaged mean flow as the base state for global stability analysis is able to capture the temporal frequency and associated mode shape of the primary vortical structures for roughness-induced transition. The time-averaged mean flow is therefore considered as an alternate base flow in the present work to investigate global instability for case (10*h*, 5*h*).

4.3.2. *High- and low-speed longitudinal streaks*

The high- and low-speed streaks are visualized in figure 14 by the streamwise deviation of the base flow from the Blasius solution for the three distributed roughness cases. Figure 14(*a*) shows that, for case (5*h*, 2.5*h*), the central and lateral low-speed streaks are merged with each other and form a shear layer above the roughness layer. The high-speed streaks are only induced at the first row of roughness elements and disappear within a short downstream distance due to the dense spanwise roughness distribution. In this case, the instability mechanism might be Kelvin–Helmholtz instability rather than streak instability. For case (5*h*, 5*h*), both the central and lateral streaks are observed in figure 14(*b*), behaving similarly to those in an isolated roughness case. The lateral low-speed streaks develop away from the SP with increasing downstream distance, due to the presence of the following roughness elements.

As the streamwise spacing is increased to $\lambda_x = 10h$, different behaviours of high- and low-speed streaks are seen in figure 14(*c*). In contrast to case (5*h*, 5*h*), the central low-speed streak only forms within the vicinity downstream of the cubes. The high-speed streaks induced by the first-row cubes move close to each other and collide with the following obstacles, which induces the high-speed streaks from the second-row cubes. The high-speed streaks grow and interact in the longitudinal grooves farther downstream.

4.3.3. *Eigenspectra and eigenmodes*

The leading eigenvalues for cases (5*h*, 5*h*) and (10*h*, 5*h*) at different Re_h are plotted in figure 15. For case (5*h*, 5*h*), compared with the isolated case at the same Re_h, the growth rate is larger and the temporal frequency is lower. This indicates that the distributed roughness elements lead to lower critical Re_h for linear instability to occur compared with the isolated roughness. The associated eigenmode for case (5*h*, 5*h*) is examined in
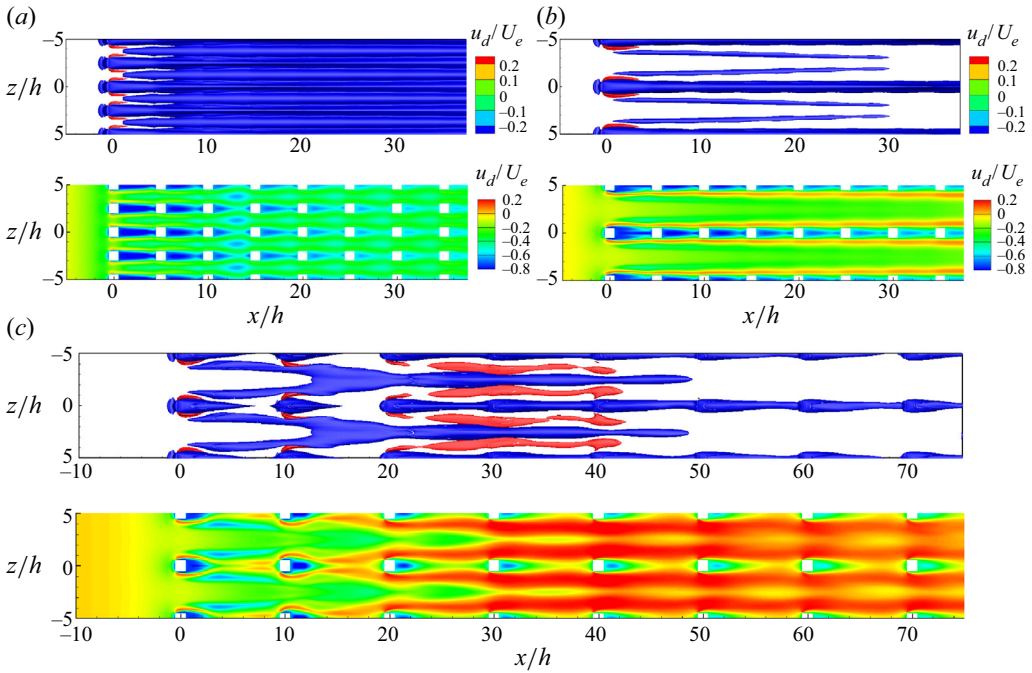
977 A27-16

Figure 14. Top-down views of high- and low-speed streaks, visualized by isosurfaces (top) and contour plots at the plane $y = 0.5h$ (bottom) of the streamwise velocity deviation of the base flow from the Blasius boundary layer solution, $u_d = U_b - u_{bl}$, for (a) case $(5h, 2.5h)$, (b) case $(5h, 5h)$ and (c) case $(10h, 5h)$. The contour levels in (c) are the same as (a,b).
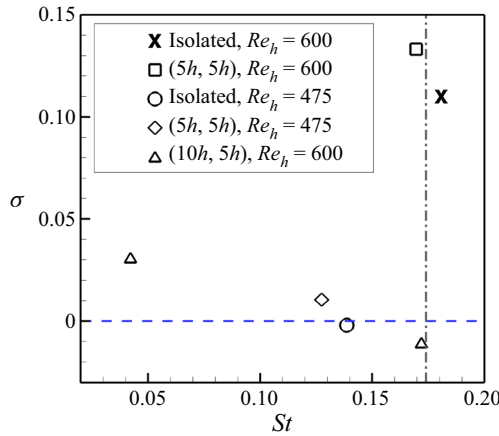

Figure 15. Leading eigenvalues for cases $(5h, 5h)$ and $(10h, 5h)$ at different Re_h, and a comparison with the isolated roughness case. The vertical dash-dot line denotes the Strouhal number $St = \omega_a h/(2\pi u_h)$ of the primary hairpin vortices, where u_h is the Blasius velocity at the roughness tips.

figure 16. The varicose mode is observed along the central low-speed streak, similar to the varicose mode observed in the isolated case (Ma & Mahesh 2022). The dominant production terms of disturbance kinetic energy P_y and P_z are examined in figure 17. This shows that the unstable mode extracts energy from both the wall-normal and spanwise
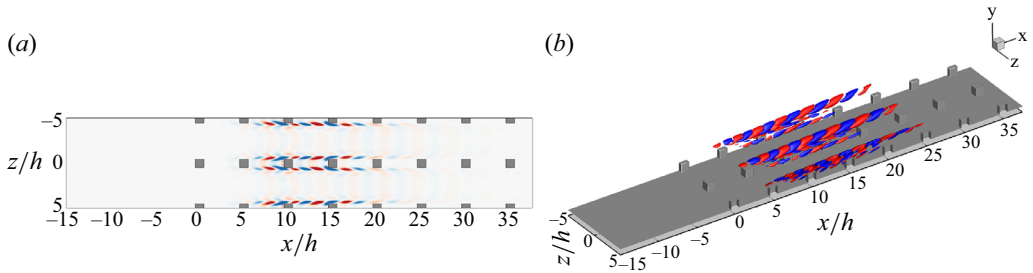
Figure 16. Contour plots in the plane of $y = 0.5h$ (a) and isosurfaces (b) of the streamwise velocity component of the leading unstable mode for case (5h, 5h) at $Re_h = 600$. The contour levels depict $\pm 10\%$ of the mode's maximum streamwise velocity.
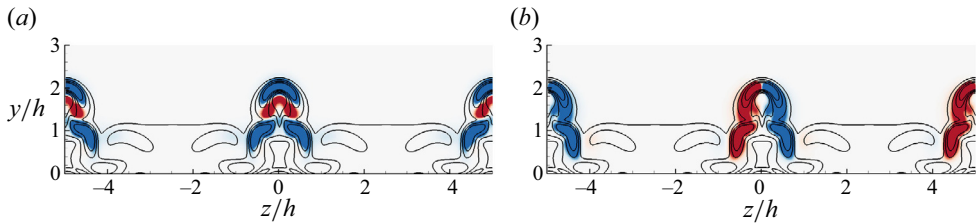

Figure 17. Contour plots of $P_y = -|\hat{u}||\hat{v}|\partial \bar{u}/\partial y$ (a) and $P_z = -|\hat{u}||\hat{w}|\partial \bar{u}/\partial z$ (b) in the cross-flow plane of $x = 12.5h$ for case (5h, 5h) at $Re_h = 600$. The contour levels depict $\pm 10\%$ of the maximum P_y and P_z. The localized shear is depicted by the solid lines of $u_s = ((\partial \bar{u}/\partial y)^2 + (\partial \bar{u}/\partial z)^2)^{1/2}$ from 0 to 2.

shears of the central low-speed streak, as well as the localized shear layer induced by the cubes.

For case (10h, 5h), two leading eigenvalues are captured in figure 15. One is the leading eigenvalue whose temporal frequency is close to that of the isolated case and case (5h, 5h). This leading eigenvalue corresponds to the primary hairpin vortex shedding and is marginally stable, consistent with the state of marginal stability of mean flow for the isolated roughness suggested by Ma & Mahesh (2022). The corresponding eigenmode in figure 18 is associated with the high-speed streaks in the longitudinal grooves as well as the entire shear layer formed above the roughness tips. The production results in figure 19 indicate that the mode extracts most of the energy from the localized shear caused by obstacles and the high-speed streaks in the grooves farther downstream. In contrast to the isolated case and case (5h, 5h), the mode hardly extracts the energy from the central low-speed streak since the central streak is diminished for larger streamwise spacing. The other unstable leading eigenvalue with a lower frequency is also obtained for case (10h, 5h) in figure 15. Figure 20 shows that the associated eigenmode displays sinuous symmetry, it is induced by the second row of roughness elements and fades away within a short downstream distance. This indicates that when the streamwise spacing is much larger than the region of flow separation, an additional unstable mode is generated as the wake flow from the first-row roughness impinges on the following roughness. The production results in figure 21 demonstrate that this sinuous mode mainly extracts its energy from the spanwise shear induced between the high- and low-speed streaks in the grooves.
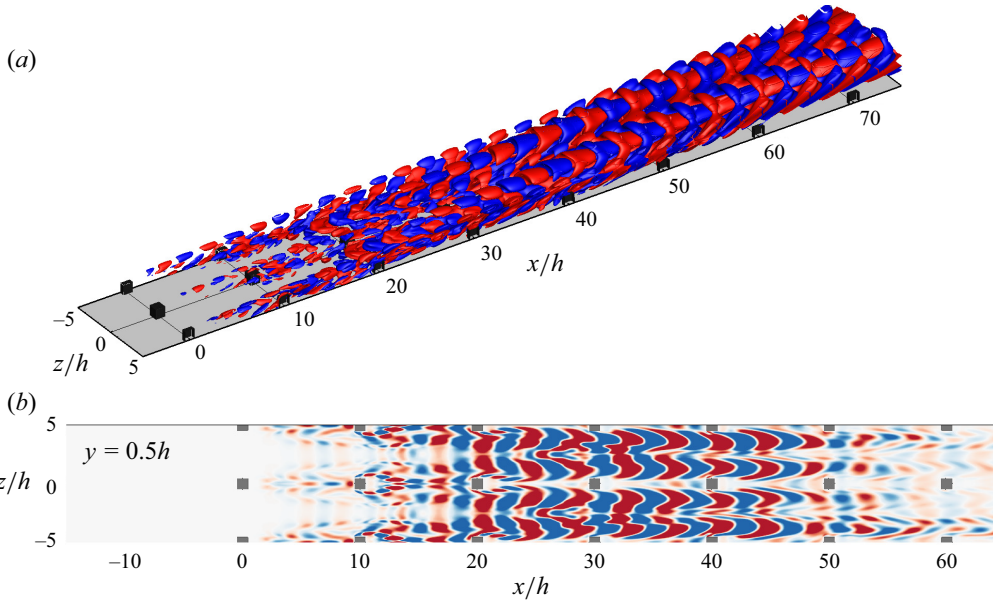
977 A27-18

Figure 18. Isosurfaces (*a*) and contour plots at $y = 0.5h$ (*b*) of the streamwise velocity component of the leading varicose mode for case $(10h, 5h)$ at $Re_h = 600$.
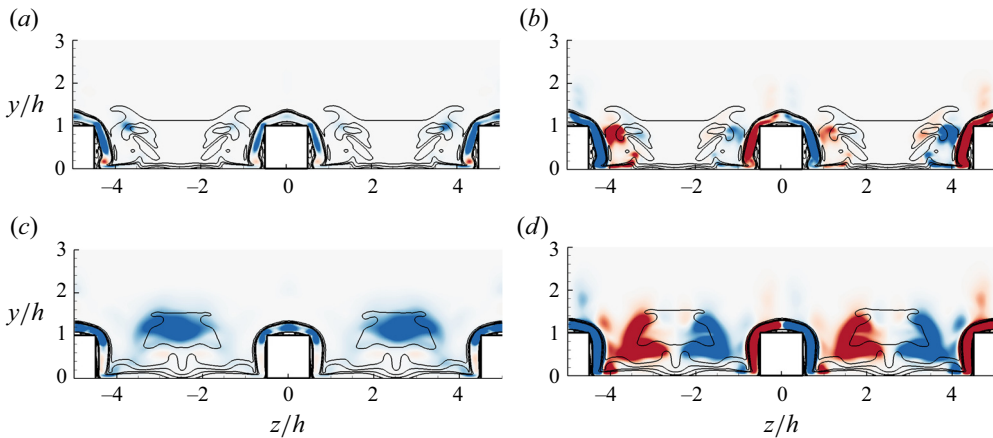

Figure 19. Contour plots of P_y (*a*,*c*) and P_z (*b*,*d*) in the cross-flow planes at (*a*,*b*) $x = 10h$ and (*c*,*d*) $x = 20h$ for the leading varicose mode of case $(10h, 5h)$ at $Re_h = 600$. The contour levels are the same as figure 17.

5. Conclusion and discussion

The effects of roughness spacing on boundary layer transition due to distributed surface roughness are investigated. Both streamwise and spanwise proximities of roughness elements are considered. The transitional flow behaviour and the primary vortical structures due to distributed surface roughness are examined by performing DNSs. Global stability analysis is performed to study the stability properties of the flow field modified by the distributed roughness, and a comparison with an isolated roughness element of the same geometry (Ma & Mahesh 2022) is made.
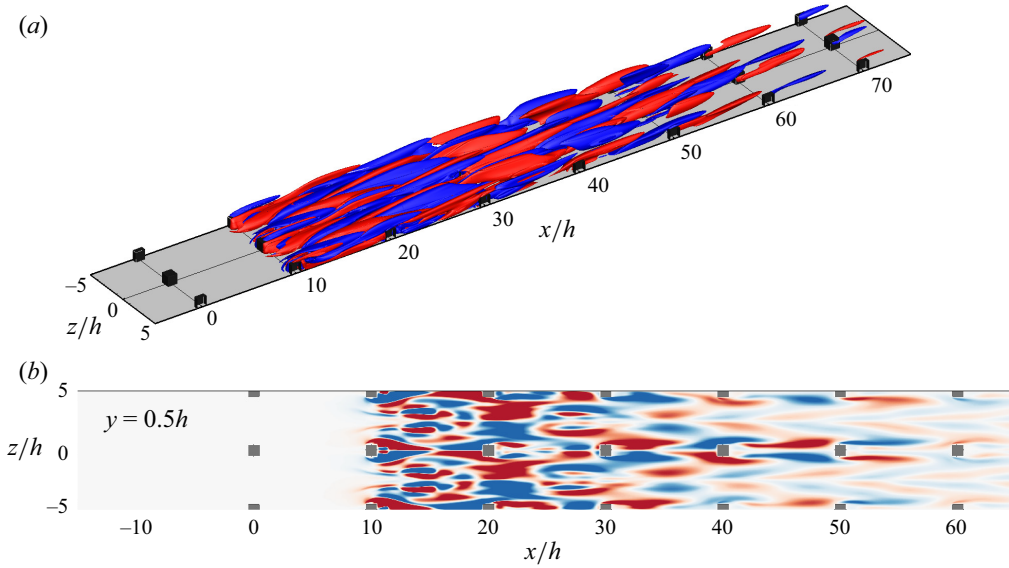
Figure 20. Isosurfaces (*a*) and contour plots at $y = 0.5h$ (*b*) of the streamwise velocity component of the leading sinuous mode for case $(10h, 5h)$ at $Re_h = 600$.
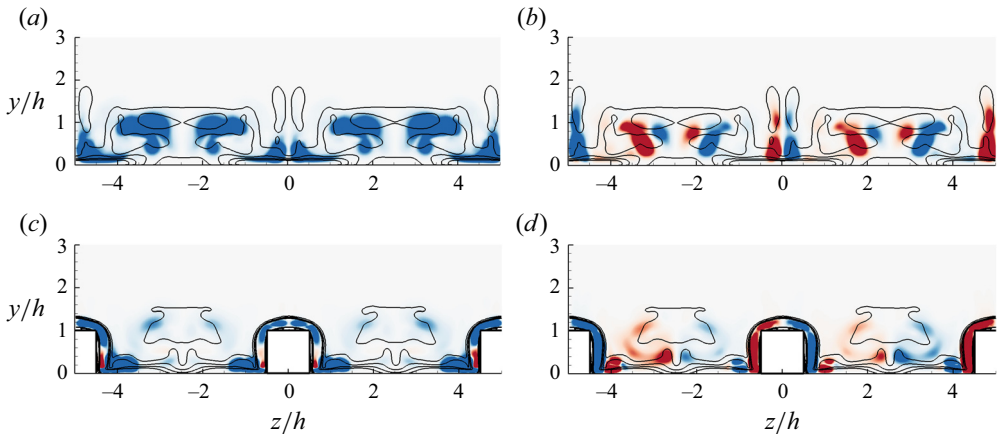

Figure 21. Contour plots of P_y (*a,c*) and P_z (*b,d*) in the cross-flow planes at (*a,b*) $x = 15h$ and (*c,d*) $x = 20h$ for the leading sinuous mode of case $(10h, 5h)$ at $Re_h = 600$. The contour levels are the same as figure 17.

The small spanwise spacing prevents transition and streak instability in the downstream boundary layer by inhibiting the formation of CVP. With the absence of CVP, the hairpin vortices are not generated and the downstream shear layer remains steady at $Re_h = 600$. The flow can be unstable at higher Re_h due to Kelvin–Helmholtz instability, which is different from the instability mechanism in the isolated case. When the spanwise spacing increases to $\lambda_z = 5h$, the hairpin vortices are generated and the roughness wake becomes unsteady. The breakdown of the boundary layer is more significant for distributed surface roughness than the isolated roughness, and a lower critical Re_h for instability to occur is found for distributed roughness.

977 A27-20

The effects of streamwise spacing are investigated for the fixed $\lambda_z = 5h$. When $\lambda_x = 5h$, the cavities sustain recirculation vortices that isolate the outer flow from the roughness. As a result, the primary hairpin vortices induced by the first-row elements behave similarly to those in the isolated case, and the leading unstable mode is consistent with that induced by the isolated roughness. The following roughness elements lead to the wake extension by generating recirculation bubbles in the wake flow, and they persistently induce disturbances to the downstream shear layer that make a contribution to the unstable nature of the wake flow. When the streamwise spacing increases to $\lambda_x = 10h$, the high-momentum fluid transfers downward into the cavities. The roughness wake from the elements in the front has an impact on the following elements, which induces different unstable modes and interactions among different perturbation modes.

Based on the comparison between isolated and distributed roughness with the same configuration parameters, the present study indicates that the dominant unstable mode and the behaviour of the primary hairpin vortices mainly depend on the initial configuration parameters of the first-row roughness elements. Roughness spacing plays an important role in modifying the unstable nature of the wake flow. For surface roughness with different distributions and initial δ^*/h, the dominant instability mechanism can be presumed from that in the isolated case, and the roughness spacing effects on the wake flow would be analogous.

Author ORCIDs.

Rong Ma https://orcid.org/0000-0002-0630-5345;

Krishnan Mahesh https://orcid.org/0000-0003-0927-5302.

REFERENCES

ÅKERVIK, E., BRANDT, L., HENNINGSON, D.S., HŒPFFNER, J., MARXEN, O. & SCHLATTER, P. 2006 Steady solutions of the Navier–Stokes equations by selective frequency damping. *Phys. Fluids* **18** (6), 068102.

ASHRAFIAN, A., ANDERSSON, H.I. & MANHART, M. 2004 DNS of turbulent flow in a rod-roughened channel. *Intl J. Heat Fluid Flow* **25** (3), 373–383.

BAKER, C.J. 1979 The laminar horseshoe vortex. *J. Fluid Mech.* **95** (2), 347–367.

BUCCI, M.A., CHERUBINI, S., LOISEAU, J.-CH. & ROBINET, J.-CH. 2021 Influence of freestream turbulence on the flow over a wall roughness. *Phys. Rev. Fluids* **6** (6), 063903.

CASACUBERTA, J., GROOT, K.J., TOL, H.J. & HICKEL, S. 2018 Effectivity and efficiency of selective frequency damping for the computation of unstable steady-state solutions. *J. Comput. Phys.* **375**, 481–497.

CASTRO, I.P. & ROBINS, A.G. 1977 The flow around a surface-mounted cube in uniform and turbulent streams. *J. Fluid Mech.* **79** (2), 307–335.

CHOUDHARI, M. & FISCHER, P. 2006 Roughness induced transient growth: nonlinear effects. In *IUTAM Symposium on Laminar-Turbulent Transition*, pp. 237–242. Springer.

CHOUDHARI, M., LI, F., CHANG, C., EDWARDS, J., KEGERISE, M. & KING, R. 2010 Llaminar-turbulent transition behind discrete roughness elements in a high-speed boundary layer. In *48th AIAA Aerospace Sciences Meeting Including the New Horizons Forum and Aerospace Exposition*, p. 1575.

CITRO, V., GIANNETTI, F., LUCHINI, P. & AUTERI, F. 2015 Global stability and sensitivity analysis of boundary-layer flows past a hemispherical roughness element. *Phys. Fluids* **27** (8), 084110.

COCEAL, O., THOMAS, T.G., CASTRO, I.P. & BELCHER, S.E. 2006 Mean flow and turbulence statistics over groups of urban-like cubical obstacles. *Boundary-Layer Meteorol.* **121** (3), 491–519.

COHEN, J., KARP, M. & MEHTA, V. 2014 A minimal flow-elements model for the generation of packets of hairpin vortices in shear flows. *J. Fluid Mech.* **747**, 30–43.

CORKE, T.C., BAR-SEVER, A. & MORKOVIN, M.V. 1986 Experiments on transition enhancement by distributed roughness. *Phys. Fluids* **29** (10), 3199–3213.

DE TULLIO, N., PAREDES, P., SANDHAM, N.D. & THEOFILIS, V. 2013 Laminar–turbulent transition induced by a discrete roughness element in a supersonic boundary layer. *J. Fluid Mech.* **735**, 613–646.

VON DEYN, L.H., FOROOGHI, P., FROHNAPFEL, B., SCHLATTER, P., HANIFI, A. & HENNINGSON, D.S. 2020 Direct numerical simulations of bypass transition over distributed roughness. *AIAA J.* **58** (2), 702–711.

ERGIN, F.G. & WHITE, E.B. 2006 Unsteady and transitional flows behind roughness elements. *AIAA J.* **44** (11), 2504–2514.

FRANSSON, J.H.M., BRANDT, L., TALAMELLI, A. & COSSU, C. 2004 Experimental and theoretical investigation of the nonmodal growth of steady streaks in a flat plate boundary layer. *Phys. Fluids* **16** (10), 3627–3638.

FRANSSON, J.H.M., BRANDT, L., TALAMELLI, A. & COSSU, C. 2005 Experimental study of the stabilization of Tollmien–Schlichting waves by finite amplitude streaks. *Phys. Fluids* **17** (5), 054110.

HUNT, J.C.R., WRAY, A.A. & MOIN, P. 1988 Eddies, streams, and convergence zones in turbulent flows. In *Studying Turbulence Using Numerical Simulation Databases, 2. Proceedings of the 1988 Summer Program*.

IKEDA, T. & DURBIN, P.A. 2007 Direct simulations of a rough-wall channel flow. *J. Fluid Mech.* **571**, 235–263.

IYER, P.S. & MAHESH, K. 2013 High-speed boundary-layer transition induced by a discrete roughness element. *J. Fluid Mech.* **729**, 524–562.

JIMÉNEZ, J. 2004 Turbulent flows over rough walls. *Annu. Rev. Fluid Mech.* **36**, 173–196.

JIMÉNEZ, J.M., REYNOLDS, R.T. & SMITS, A.J. 2010 The effects of fins on the intermediate wake of a submarine model. *Trans. ASME J. Fluids Engng* **132** (3), 031102.

JORDI, B.E., COTTER, C.J. & SHERWIN, S.J. 2014 Encapsulated formulation of the selective frequency damping method. *Phys. Fluids* **26** (3), 034101.

LEONARDI, S. & CASTRO, I.P. 2010 Channel flow over large cube roughness: a direct numerical simulation study. *J. Fluid Mech.* **651**, 519–539.

LOISEAU, J., ROBINET, J., CHERUBINI, S. & LERICHE, E. 2014 Investigation of the roughness-induced transition: global stability analyses and direct numerical simulations. *J. Fluid Mech.* **760**, 175–211.

MA, R., ALAMÉ, K. & MAHESH, K. 2021 Direct numerical simulation of turbulent channel flow over random rough surfaces. *J. Fluid Mech.* **908**, A40.

MA, R. & MAHESH, K. 2022 Global stability analysis and direct numerical simulation of boundary layers with an isolated roughness element. *J. Fluid Mech.* **949**, A12.

MAHESH, K., CONSTANTINESCU, G. & MOIN, P. 2004 A numerical method for large-eddy simulation in complex geometries. *J. Comput. Phys.* **197** (1), 215–240.

MORSE, N., KROLL, T. & MAHESH, K. 2022 Large-eddy simulation of submerged marine vehicles. In *34th Symposium on Naval Hydrodynamics*.

MOSER, R.D., KIM, J. & MANSOUR, N.N. 1999 Direct numerical simulation of turbulent channel flow up to $Re_\tau = 590$. *Phys. Fluids* **11** (4), 943–945.

MUPPIDI, S. & MAHESH, K. 2012 Direct numerical simulations of roughness-induced transition in supersonic boundary layers. *J. Fluid Mech.* **693**, 28–56.

PERRY, A.E., SCHOFIELD, W.H. & JOUBERT, P.N. 1969 Rough wall turbulent boundary layers. *J. Fluid Mech.* **37** (2), 383–413.

PLASSERAUD, M., KUMAR, P., MA, R. & MAHESH, K. 2022 Simulation of flow over an inclined spheroid at high Reynolds number: tripping effects. In *34th Symposium on Naval Hydrodynamics*.

PLASSERAUD, M., KUMAR, P. & MAHESH, K. 2023 Large-eddy simulation of tripping effects on the flow over a 6 : 1 prolate spheroid at angle of attack. *J. Fluid Mech.* **960**, A3.

PUCKERT, D.K. & RIST, U. 2018 Experiments on critical Reynolds number and global instability in roughness-induced laminar-turbulent transition. *J. Fluid Mech.* **844**, 878–903.

RESHOTKO, E. 2001 Transient growth: a factor in bypass transition. *Phys. Fluids* **13** (5), 1067–1075.

TANI, I. 1987 Turbulent boundary layer development over rough surfaces. In *Perspectives in Turbulence Studies*, pp. 223–249. Springer.

THEOFILIS, V. 2011 Global linear instability. *Annu. Rev. Fluid Mech.* **43**, 319–352.

VADLAMANI, N.R., TUCKER, P.G. & DURBIN, P. 2018 Distributed roughness effects on transitional and turbulent boundary layers. *Flow Turbul. Combust.* **100** (3), 627–649.

VANDERWEL, C. & GANAPATHISUBRAMANI, B. 2015 Effects of spanwise spacing on large-scale secondary flows in rough-wall turbulent boundary layers. *J. Fluid Mech.* **774**, R2.

XIE, Z. & FUKA, V. 2018 A note on spatial averaging and shear stresses within urban canopies. *Boundary-Layer Meteorol.* **167** (1), 171–179.

XU, H., ALTLAND, S.J., YANG, X. & KUNZ, R.F. 2021 Flow over closely packed cubical roughness. *J. Fluid Mech.* **920**, A37.